crystals

MDPI

Article

Plasmonic Au–Pd Bimetallic Nanocatalysts for Hot-Carrier-Enhanced Photocatalytic and Electrochemical Ethanol Oxidation

Jonathan Boltersdorf [1,*], Asher C. Leff [1,2], Gregory T. Forcherio [1,3] and David R. Baker [1]

[1] United States Army Research Laboratory, Sensors and Electron Devices Directorate, Adelphi, MD 20783, USA; asher.c.leff.ctr@mail.mil (A.C.L.); gregory.forcherio@navy.mil (G.T.F.); david.r.baker175.civ@mail.mil (D.R.B.)
[2] General Technical Services, Wall, NJ 07727, USA
[3] Electro-Optic Technology Division, Naval Surface Warfare Center, Crane, IN 47522, USA
* Correspondence: jonathan.a.boltersdorf.civ@mail.mil

Abstract: Gold–palladium (Au–Pd) bimetallic nanostructures with engineered plasmon-enhanced activity sustainably drive energy-intensive chemical reactions at low temperatures with solar simulated light. A series of alloy and core–shell Au–Pd nanoparticles (NPs) were prepared to synergistically couple plasmonic (Au) and catalytic (Pd) metals to tailor their optical and catalytic properties. Metal-based catalysts supporting a localized surface plasmon resonance (SPR) can enhance energy-intensive chemical reactions via augmented carrier generation/separation and photothermal conversion. Titania-supported Au–Pd bimetallic (i) alloys and (ii) core–shell NPs initiated the ethanol (EtOH) oxidation reaction under solar-simulated irradiation, with emphasis toward driving carbon–carbon (C–C) bond cleavage at low temperatures. Plasmon-assisted complete oxidation of EtOH to CO_2, as well as intermediary acetaldehyde, was examined by monitoring the yield of gaseous products from suspended particle photocatalysis. Photocatalytic, electrochemical, and photoelectrochemical (PEC) results are correlated with Au–Pd composition and homogeneity to maintain SPR-induced charge separation and mitigate the carbon monoxide poisoning effects on Pd. Photogenerated holes drive the photo-oxidation of EtOH primarily on the Au-Pd bimetallic nanocatalysts and photothermal effects improve intermediate desorption from the catalyst surface, providing a method to selectively cleave C–C bonds.

Keywords: plasmonic resonance; catalytic energy conversion; nanomaterials

Citation: Boltersdorf, J.; Leff, A.C.; Forcherio, G.T.; Baker, D.R. Plasmonic Au–Pd Bimetallic Nanocatalysts for Hot-Carrier-Enhanced Photocatalytic and Electrochemical Ethanol Oxidation. *Crystals* **2021**, *11*, 226. https://doi.org/10.3390/cryst11030226

Academic Editor: Duncan Gregory

Received: 22 January 2021
Accepted: 20 February 2021
Published: 25 February 2021

1. Introduction

Efficient chemical transformations of readily available resources (solar energy, water, waste products, etc.) via light-energy conversion enables the generation of energy-dense fuels and electrical power [1–3]. Directed harvesting of solar energy can be facilitated by photocatalytic processes augmented by plasmon-mediated chemistry [3–8]. Plasmonic nanostructures (Au, Ag) exhibit localized surface plasmon resonance (SPR), the coherent oscillation of conduction electrons coupled to strong local electric fields. Landau damping of the SPR (1–100 fs) promotes excitation of energetic, or "hot", charge carriers [3,8,9], in addition to increasing light absorption, enhancing far-field light scattering, and inducing charge separation in semiconductors [3,6,8–10]. Ohmic relaxation of "hot" electrons (100 fs to 1 ps) results in local thermal dissipation (100 ps to 10 ns) that can aid in activating adsorbed reactants and accelerating surface kinetics [3,9,10]. Emerging multifunctional photocatalysts incorporate both plasmonic and catalytic active materials for chemical conversion [3,5–16]. Coupling of plasmonic metals to semiconductors as a photosensitization

strategy has demonstrably facilitated hot-carrier generation/separation [6,7,11,12]. Bimetallic nanocatalysts with a plasmonic component interact strongly with resonant photons, generating hot carriers at catalytically active noble metal sites to promote chemical transformations and enhance product selectivity [16–18]. Previous reports postulate that surface charge heterogeneity and transfer in bimetallic nanostructures can strengthen reactant adsorption, enhance product selectivity [4,5,19–21], and increase the rate of H_2 production [4,22–29]. Strategically engineered bimetallic nanocatalysts present a transformative pathway to control electronic and optical properties to overcome current limitations in catalysis and selectively enhance reactions, such as the ethanol (EtOH) oxidation reaction (EOR).

EtOH is an attractive nontoxic chemical fuel owing to its existing supply chain, carbon-neutral production from agricultural biomass, high theoretical energy density (~8 $kWh \cdot kg^{-1}$), and simple storage and infrastructure [2,30–32]. Further, the EOR has the capability for H_2 generation via catalytic deprotonation under neutral to acidic conditions. The desired EOR pathway is a high-energy ($\Delta G = -1326.7$ kJ/mol), 12-electron process that requires multiple electron transfer steps for the C_1-overall reaction(s) in low and high pH [2]:

$$\text{[Low pH]}\ CH_3CH_2OH + 3H_2O \rightarrow 2CO_2 + 6H_2 + 12e^- \quad (1)$$

$$\text{[High pH]}\ CH_3CH_2OH + 16OH^- \rightarrow 2CO_3^{2-} + 11H_2O + 12e^- \quad (2)$$

Breaking the carbon–carbon (C–C) bond has been found to be the rate-limiting step, as the EOR is interrupted by the production of two C_2-intermediates: acetaldehyde (CH_3CHO, $n = 2e^-$) first, and then further by acetic acid (CH_3COOH, $n = 4e^-$). The C_2-intermediate(s) can obstruct active sites by adsorbing in inactive orientations and possess high energetic barriers for cleaving the C–C bond (>1.0 eV); limiting further oxidation [30,32–34].

$$\text{[Low pH]}\ CH_3CH_2OH \rightarrow CH_3CHO + 2H^+ + 2e^- \quad (3)$$

$$CH_3CH_2OH + H_2O \rightarrow CH_3COOH + 4H^+ + 4e^- \quad (4)$$

$$\text{[High pH]}\ CH_3CH_2OH + 2OH^- \rightarrow CH_3CHO + 2H_2O + 2e^- \quad (5)$$

$$CH_3CH_2OH + 5OH^- \rightarrow CH_3COO^- + 4H_2O + 4e^- \quad (6)$$

Alkaline media (pH ≥ 14) enables preferred deprotonation of the sterically hindered acetaldehyde intermediate to the $[CH_2CHO]^-$ anion ($pK_a = 13.6$) and facilitates proper surface alignment for C–C bond cleavage [2,25,30,32,34]. Therefore, the complexity of the EOR necessitates that the catalyst of interest can selectively activate C–C bond cleavage for complete oxidation. The reaction rate for Au is dependent on the deprotonation step, whereas further oxidation is deterministic for catalytic metals (i.e., Pd). Therefore, Pd is one of the most active catalysts for the EOR, while Au is considered to have poor activity [25,30,33,34]. However, the catalytically active Pd lacks a strong SPR absorption for visible-light excitation and is susceptible to catalyst poisoning. Alloying or coupling Pd with plasmonic metals has shown improved catalytic reactivity compared to mono-metallic alternatives [5,20,28], and is hypothesized to enhance the EOR activity.

The coupling of plasmonic and catalytic metals to semiconductive TiO_2 is a cost-effective alternative to using pure Pd catalysts to address challenges associated with product selectivity and total conversion of EtOH. This work leverages high-resolution electron imaging techniques (i.e., STEM), photocatalytic and PEC measurements of EOR, and discrete dipole approximation (DDA) computation to provide new, quantitative insights into understanding the role of plasmonic "hot" carriers in C–C bond cleavage during the EOR [35,36]. The synthetic preparation of bimetallic nanoparticles synergistically couples Au

plasmonic absorbers with catalytic Pd, with the goal of tailoring their optical and catalytic properties. The effects of composition (i.e., $Au_{1-x}Pd_x$) and nanostructuring of the bimetallic nanoparticles (i.e., alloy vs. core–shell) on the plasmonic enhancement of the wide band gap TiO_2 are presented. Low-temperature photo-oxidation of EtOH was studied via suspended particle photocatalysis and electrochemical methods, with EOR performance directly correlated to alloy homogeneity. Plasmonic catalyst structural and elemental morphologies were optimized to improve "hot" carrier generation and separation.

2. Materials and Methods

2.1. Chemicals

Polyvinylpyrrolidone (PVP-40, 40,000 g/mol, Sigma-Aldrich, St. Louis, MI, USA), H_2PdCl_4 (99.999%, Sigma-Aldrich), $HAuCl_4{\cdot}3H_2O$ (99.999%, Sigma-Aldrich), L-ascorbic acid (> 99%, Alfa Aesar, Ward Hill, MA, USA), TiO_2 (P25 ≈ 25 nm, Evonik, Essen, Germany), anhydrous ethyl alcohol (EtOH, 200 proof, Sigma-Aldrich), Vulcan XC-72 carbon black powder (Cabot, Boston, MA, USA), tert-butylamine (t-BuNH_2, ≥ 99.0%, Sigma-Aldrich), Nafion 117 solution (Nafion, 5% in 1:1 EtOH:H_2O), $HClO_4$, HCl, and KOH were used as received, without further purification. Distilled, deionized water (18.2 MΩ·cm, EasyPure RF D7031) was utilized in all syntheses and measurements.

2.2. Nanoparticle Synthesis

2.2.1. Gold–Palladium Alloys

Gold–palladium bimetallic alloy nanoparticles ($Au_{1-x}Pd_x$ NPs) were prepared with the compositions Au, $Au_{0.9}Pd_{0.1}$, $Au_{0.75}Pd_{0.25}$, $Au_{0.5}Pd_{0.5}$, $Au_{0.25}Pd_{0.75}$, $Au_{0.1}Pd_{0.9}$, and Pd using a protocol reported in Reference [5]. First, the dark orange Pd precursor solution, 10 mM H_2PdCl_4, was prepared following our previously reported methodology [5,28]. Briefly, the desired compositions of the $Au_{1-x}Pd_x$ NP growth solutions were achieved by appropriately adjusting the mole ratio of 10 mM $HAuCl_4{\cdot}3H_2O$ and/or 10 mM H_2PdCl_4. Surfactant solution utilized to direct bimetallic alloy NP growth was 25 μM PVP-40 in 20% EtOH/80% deionized water. Precursors were combined with the surfactant solution to yield an orange-colored growth solution. A fresh solution of 0.100 M ascorbic acid was prepared and 110 μL was added to the growth solution as a weak reducing agent, which was stirred for 60 min at 100 °C. The solution colors ranged from red to brown, yielding the desired $Au_{1-x}Pd_x$ NP compositions [5].

2.2.2. Gold–Palladium Core–Shells

Similarly, the standard protocol previously reported in detail in Reference [5] was used for the growth of gold nanospheres (AuNSs) as starting materials for core–shell nanoparticles (Au_{Core}–$Au_{1-x}Pd_{x,Shell}$ NPs). AuNSs were grown by combining 10 mM $HAuCl_4{\cdot}3H_2O$, the PVP-40 surfactant solution in 20% EtOH, and 110 μL of 0.100 M ascorbic acid, which was stirred for 60 min at 30 °C to yield a red-colored AuNS solution. AuNSs were subsequently combined with 10 mM H_2PdCl_4 and 0.100 M ascorbic acid for a 10 mol% Pd shell loading (Au_{Core}–10% Pd_{Shell} NPs). Similarly, the AuNSs were combined with 10 mM H_2PdCl_4, 10 mM $HAuCl_4{\cdot}3H_2O$, and 0.100 M ascorbic acid to yield a 10 mol% $Au_{0.5}Pd_{0.5}$ shell loading (Au_{Core}–10% $AuPd_{Shell}$ NPs). Solution changed from bright red to a darker red as Pd and AuPd shells formed on the AuNSs. $Au_{1-x}Pd_x$ and Au_{Core}–$Au_{1-x}Pd_{x,Shell}$ NPs were collected by a centrifugation and washing procedure [5,6,28], followed by dispersion of the $Au_{1-x}Pd_x$ and Au_{Core}–$Au_{1-x}Pd_{x,Shell}$ bimetallic NPs in EtOH, which were stored in refrigeration.

2.2.3. Deposition of Au–Pd on Catalyst Supports

After purification, the Au–Pd NP samples were deposited onto TiO_2 and carbon supports. TiO_2 was mixed with 1 wt.% Au–Pd NPs, sonicated to thoroughly disperse, and the well-mixed slurry was stirred for 48 h. Au–Pd NPs dispersed on TiO_2 were collected using

a centrifugation and washing procedure (at 8500 rpm for 45 min). Supernatant was tested via ultraviolet-visible (UV–Vis) spectroscopy after washing to confirm the complete deposition of Au–Pd NPs onto TiO_2. Samples were dried at 80 °C for 24 h to remove excess solvent, yielding uniform powders ranging from purple to dark gray in color. Au–Pd NP samples were deposited onto XC-72 carbon supports via ligand-exchange-induced destabilization. An NP loading of 1–20 wt.% by total mass of Au and/or Pd (assuming a theoretical yield of 100%) was used for each XC-72 support. XC-72 carbon powder was added to 15 mL of t-$BuNH_2$ and thoroughly dispersed via ultrasonication. Previously prepared Au–Pd NP samples were redispersed in EtOH, mixed with XC-72/$BuNH_2$ suspension, and stirred magnetically for 24 h for ligand exchange and NP deposition. Au–Pd NPs on carbon supports were isolated via 30 mL EtOH addition and centrifugation (8500 rpm for 45 min) and dried at 80 °C.

2.2.4. Working Electrode Preparation

Catalyst suspensions were prepared by dispersing the TiO_2- and carbon-supported Au–Pd in 1:1 EtOH:H_2O and 1 vol% Nafion solution via ultrasonication for 15 min to obtain a final catalyst concentration of 6 $\mu g \cdot \mu L^{-1}$. The catalyst suspension (10 μL) was drop-cast onto a glassy carbon electrode (0.196 cm^{-2}). After excess solvent evaporation, 3 μL of a diluted Nafion solution (20% *v*/*v* in EtOH) was deposited onto the catalyst layer to improve its physical stability and electrical conductivity. Electrode surfaces were allowed to completely dry prior to EOR electrochemical measurements.

2.3. Characterization

2.3.1. UV–Vis Spectroscopy and Electron Microscopy

Absorbance spectra collected from UV to near-infrared (NIR) for the $Au_{1-x}Pd_x$ and $Au_{Core}–Au_{1-x}Pd_{x,Shell}$ NPs in solution were obtained with an AvaSpec-ULS2048L spectrometer fiber-coupled deuterium and halogen light source, while diffuse reflectance measurements of the Au–Pd on TiO_2 powders required the addition of an Avasphere-30 PTFE integrating sphere. Bright-field TEM and high-angle annular dark-field imaging scanning TEM (HAADF-STEM) was performed in JEOL 2100F (Peabody, MA, USA) at 200 kV equipped with an EDAX Octane T Optima system (Mahwah, NJ, USA) energy dispersive X-ray spectrometer (EDXS) to map the elemental distribution on the Au–Pd on TiO_2 composites. Principal component analysis differentiated raw EDS spectra into six uncorrelated variables: Au, Pd, Ti, O, C (the support film), and background (surfactant, residual solvent, etc.). Samples were prepared by drop-casting onto solid carbon films for the $Au_{1-x}Pd_x$ and $Au_{Core}–Au_{1-x}Pd_{x,Shell}$ NPs and lacey carbon films for the Au–Pd on TiO_2 powders.

2.3.2. X-ray Photoelectron Spectroscopy

X-ray photoelectron spectroscopy (XPS) was carried out on a Physical Electronics VersaProbe III (East Chanhassen, MN, USA) with a monochromated Al Kα source with a 100 μm diameter 25 W beam, 55 eV pass energy, and a take-off angle of 45°. Surface charging was neutralized by a low-voltage Ar-ion beam and a barium oxide neutralizer. Spectra were energetically corrected to a 284.8 eV C 1s line and baseline corrected to a Shirley model. Peak fitting was performed with Physical Electronics' MultiPak software v9.6.0.15. Samples were prepared by drop-casting 5 μL of NP−solvent solution onto glass substrates.

2.3.3. Numerical Computation

Electric near-field enhancements and SPR properties were studied and quantified using the discrete dipole approximation (DDA) package DDSCAT v7.3 by Draine and Flatau [37–39]. DDA uses Maxwell's equations to quantify absorption and scattering of an electric plane wave incident upon a subwavelength NP, discretized into a three-dimensional ensemble of point dipoles susceptible to electric polarization according to their specified dielectric response [6,28,29,40]. Nanoparticle targets were generated using a custom

MATLAB (v9.2, MathWorks, Natick, MA, USA) script based on Reference [29] according to the TEM-measured mean dimensions, with a 10 nm diameter $Au_{1-x}Pd_x$ NP and 24 nm Au_{Core}–$Au_{1-x}Pd_{x,Shell}$ NP in the presence and absence of contacting anatase TiO_2 (25 nm diameter) in water (n = 1.33). The inter-dipole spacing was 0.5 nm. The DDA models presented herein consider only the anatase phase of TiO_2 owing to both the anatase and rutile phases of TiO_2 exhibiting a nearly identical dispersive dielectric behavior in the sub-band gap visible spectrum [6]. Therefore, under sub-band gap visible-light irradiation, the anatase and rutile forms are optically equivalent as they both screen the plasmon resonance.

2.3.4. Photocatalytic Measurements

Gas chromatography–mass spectrometry–multiple headspace extraction (GC-MS-MHE) was performed on an Agilent Technologies 5975C Series GC/MSD, with Triple-Axis HED-EM Detector coupled to an Agilent 7697A Headspace Sampler utilized to perform headspace analysis of the photo-oxidation experiments. Sample vials were equilibrated at 60 °C under dark conditions for 20 minutes, and the headspace was extracted for the dark/thermal background [6]. Catalyst supports were used in all photocatalytic experiments. Photocatalytic EOR measurements of 1 wt.% Au–Pd cocatalysts loaded on TiO_2 samples (5 mg total) were performed in 0.010 M $HClO_4$ + 0.50 M EtOH. NP suspensions were irradiated in purged GC-MS-MHE glass vials excited with solar-simulated light (i.e., denoted AM1.5G) using a 300 W Xe arc-lamp. The power density for the AM1.5G experiments (> 350 nm) was set to 100 $mW \cdot cm^{-2}$ (i.e., ®~1 Sun). Photoreactor cells were irradiated for 1–4 h under constant stirring, and gaseous products were detected post-irradiation.

2.3.5. Electrochemical Measurements

Catalyst supports (i.e., TiO_2 and C) were used in all electrochemical experiments. Electrochemical rotating disk electrode (RDE) hydrodynamic measurements were performed in a three-electrode custom-made quartz cell on a Solartron potentiostat. The three electrodes utilized were an Ag/AgCl reference electrode (4 M KCl with AgCl solution), a Pt coil counter electrode (4.7 cm^2), and the Au–Pd NPs on TiO_2 and carbon support deposited on polished glassy carbon (i.e., 0.196 cm^{-2}) as the working electrodes. All measurements were temperature-controlled at 25 °C with water circulated through the outer jacket of the quartz cell. Prior to electrochemical measurements, N_2 was bubbled in solution for 30 min and then placed in the headspace to maintain the sparged solution. A sequential cycling method was used to measure the Au–Pd working electrodes in 1 M KOH supporting electrolyte at 200, 100, 50, 20, and 5 $mV \cdot s^{-1}$, with the addition of 0.50 M EtOH for the EOR measurements. For the 200, 100, and 50 $mV \cdot s^{-1}$ scan rates, the working electrodes were cycled 25 times each, whereas for the 20 and 5 $mV \cdot s^{-1}$ scan rates, the electrodes were cycled 10 and 3 times each, respectively, under rotating conditions (ω = 400 rpm) to achieve reproducible cyclic voltammograms (CV) [30]. Chronoamperometric (CA) measurements were obtained with an applied bias of + 0.72 V (vs. reversible hydrogen electrode (RHE)) for 2150 s under chopped light irradiation (250 s light on/light off). The RDEs were irradiated with solar-simulated light (i.e., AM1.5G filter).

3. Results and Discussion

3.1. Synthesis and Characterization of Au–Pd Bimetallic NPs

Gold–palladium bimetallic nanoparticles ($Au_{1-x}Pd_x$ and Au_{Cor}–$Au_{1-x}Pd_{x,Shell}$ NPs) were prepared using stock solutions of Au and Pd chloride precursor salts in a modified colloidal synthetic method with systematic variation of the composition. High-temperature (100 °C) growth conditions were used in the preparation of $Au_{1-x}Pd_x$ NPs to improve the nucleation and growth of homogeneous alloys. Alloyed $Au_{1-x}Pd_x$ NPs maintained their integrity after being coupled to the 3.2 eV bandgap semiconductor TiO_2 and were character-

ized by STEM-HAADF imaging [5] and EDXS elemental maps shown in Figure 1. Monodisperse spherical morphologies exhibited average particle diameters for Au (23.3 ± 8.7 nm), $Au_{0.9}Pd_{0.1}$ (7.3 ± 5.9 nm), $Au_{0.75}Pd_{0.25}$ (2.9 ± 0.6 nm), $Au_{0.5}Pd_{0.5}$ (5.9 ± 3.6 nm), $Au_{0.25}Pd_{0.75}$ (7.6 ± 4.5 nm), and Pd (1.7 ± 0.6 nm) determined from statistical analysis of TEM images [5]. Elemental analysis of the NPs using STEM-EDXS spectra confirmed the average composition reflects the desired loading after subtracting TiO_2 background, as shown in the Supplementary Figure S1. The Au–Pd distribution was synthetically controlled in a heterogeneous manner using core–shell growth techniques.

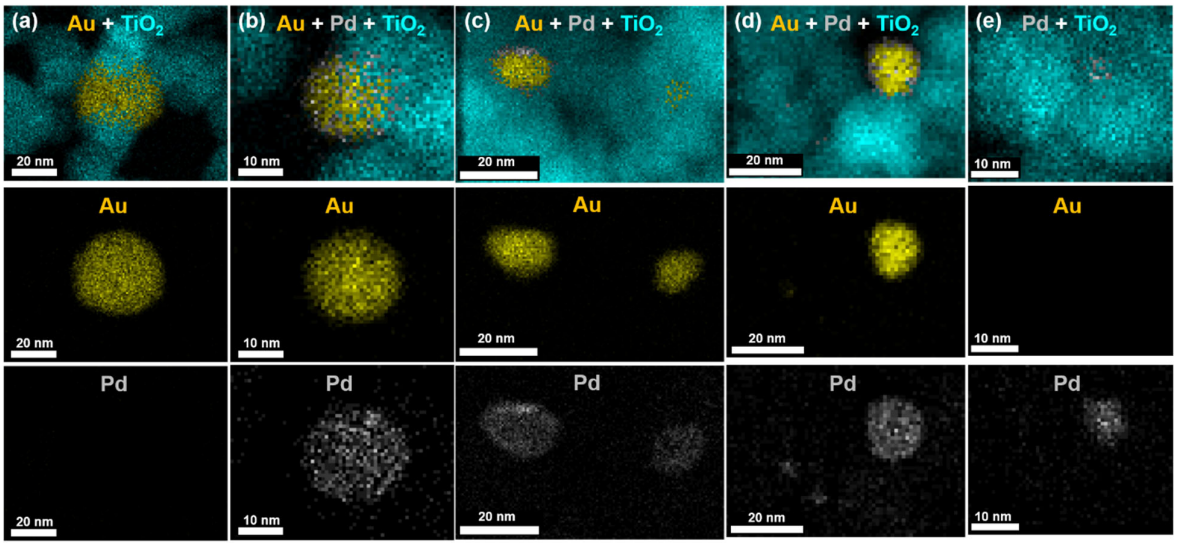

Figure 1. EDXS images taken in STEM mode representative of (**a**) Au, (**b**) $Au_{0.9}Pd_{0.1}$, (**c**) AuPd, (**d**) $Au_{0.25}Pd_{0.75}$, and (**e**) Pd NPs on a TiO_2 support, with the Au, Pd, and TiO_2 shown in yellow, gray, and teal, respectively.

Heterogeneous core–shell NPs were grown at low-temperature conditions (30 °C) in a two-step synthesis method: (1) growth of the Au NP core and (2) deposition of the desired $Au_{1-x}Pd_x$ shell. Shell thickness was varied by increasing the loading in the second synthesis step from 1 to 10 mol% for a $Au_{0.5}Pd_{0.5}$ (AuPd) and Pd shell. The two-step core–shell synthesis method resulted in homogenous, faceted icosahedron Au core NPs with thin homogeneous shells that continued the growth pattern, as shown in Figure 2. Elemental mapping of Au and Pd via EDXS, shown in Figure 2, revealed a core–shell structure with 1–2 nm AuPd and Pd thick shells. Compositions of the core–shell NPs were confirmed by STEM-EDXS, shown in Supplementary Figure S2. XPS in Figure 3 and Supplementary Figure S3 confirmed the presence of metallic Au and Pd species for the alloy and core–shell NPs by the Au 4f peaks at 83.7 and 87.4 eV and the Pd 3d peaks at 335 and 340 eV binding energies. Au exhibits convoluting 4d peaks in the binding energy region of Pd 3d as well but is suppressed with increasing Pd content. XPS analysis of the Au and Pd species for the $Au_{0.9}Pd_{0.1}$ alloy closely resembles both the Au_{Core} NPs with 10% AuPd and 10% Pd shell. XPS-measured valence band (VB) density-of-states (DOS) in Figure 3 and Supplementary Figure S4 revealed a shift in *d*-band onset toward the E_F (i.e., 0 eV binding energy) and an increase in the DOS at the E_F with an increase in Pd content, a signature of Pd observed in density functional theory (DFT) calculations and measurements of other Au–Pd bimetallics [30,35,40,41]. Modifying the position of the *d*-band center relative to the E_F for Au–Pd arises owing to the inherent properties of Pd. Additionally, mechanical strain and/or direct charge transfer between the two metals can take place in alloy and core–shell NPs; designated the ligand effect. The ligand effect can impact how molecules adsorb to the catalyst surface and subsequently modify the Au–Pd catalytic activity [18,42]. The E_F of both Au and Pd lie lower in energy in relation to the conduction

band (CB) minimum of TiO_2, with the DOS increasing at the E_F with an increase in the Pd content [43].

Compared to the alloyed $Au_{1-x}Pd_x$ NPs, the Au_{Core}–$Au_{1-x}Pd_{x,Shell}$ NPs exhibited facets with expanded average particle diameters due to secondary AuPd and Pd growth. Size distributions were determined from the statistical analysis of HAADF-STEM images and yielded average particle/shell diameters for the Au_{Core} NPs with a 10 mol% $AuPd_{Shell}$ (45.5 ± 13.9 nm overall diameter, 1.2 ± 0.5 nm shell thickness) and 10 mol% Pd_{Shell} (30.5 ± 12.6 nm overall diameter, 1.3 ± 0.6 nm shell thickness). Notably, tensile strain in the epitaxial thin shell enables the ligand effect to aid in modifying the *d*-band of the core–shell NP, which is absent for thicker shells (i.e., 7–9 nm) [18]. AuPd and Pd shell growth appeared to follow an epitaxial-like Frank–van der Merwe mode over the Au_{Core} NP in Figure 2, and was consistent with related studies [26,29]. Au_{Core}–$Au_{1-x}Pd_{x,Shell}$ NPs synthesized using the same procedure using < 10 mol% Pd yielded thinner AuPd and Pd shells with a lack of distinct crystal facets. Overall, chemical reductive deposition of thin AuPd and Pd shells onto Au_{Core} NPs yielded an epitaxial interface for optimal Au–Pd optical characteristics to promote photocatalytic charge excitation and transfer.

UV–Vis spectroscopy was used to characterize the optical properties of the $Au_{1-x}Pd_x$ and Au_{Core}–$Au_{1-x}Pd_{x,Shell}$ NPs in solution, shown in Figure 4 and Supplementary Table S1, Figures S5 and S6. Pure Au NPs exhibited a λ_{Max} of 526 nm, but the relative intensity of the plasmonic resonance rapidly decayed by 50% after incorporating 10% Pd. Au is responsible for the plasmonic response at visible wavelengths, while Pd does not support visible SPR [18]. Pd exhibits a *d*-band center closer to the E_F, causing the optical response to be dominated by interband transitions and dampen the localized SPR at all frequencies, making it spectrally broad and lower in intensity [18,28]. Therefore, the rapid dampening of the SPR with increasing Pd observed for the alloys in Figure 4a is indicative of the homogeneous mixing of Pd into Au. In contrast, the core–shell morphologies in Figure 4b retain a strong plasmonic response (λ_{Max}) at 530 nm, with linewidth expansion of the SPR peak (λ_{Max}) owing to the Pd-containing shell layers. Spectral broadening observed at longer wavelengths (> 650 nm) is attributed to Pd in the alloyed and core–shell compositions. Observable changes in the SPR were ostensibly due to the emergence of additional plasmon damping pathway(s) for the $Au_{1-x}Pd_x$ and Au_{Core}–$Au_{1-x}Pd_{x,Shell}$ NPs [36,44,45].

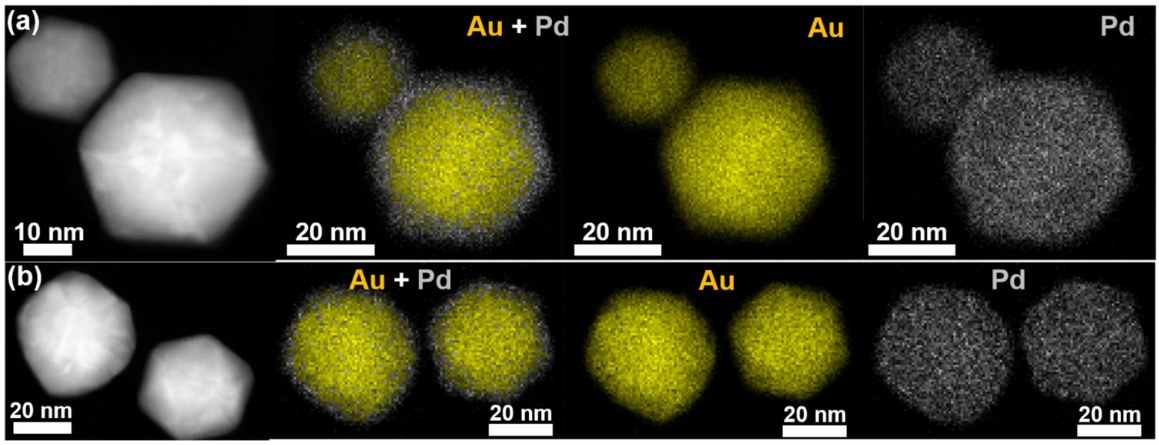

Figure 2. STEM-HAADF images and correlated EDXS maps of Au_{Core} NPs with (**a**) 10% $AuPd_{Shell}$ and (**b**) 10% Pd_{Shell}, with the Au and Pd shown in yellow and gray, respectively.

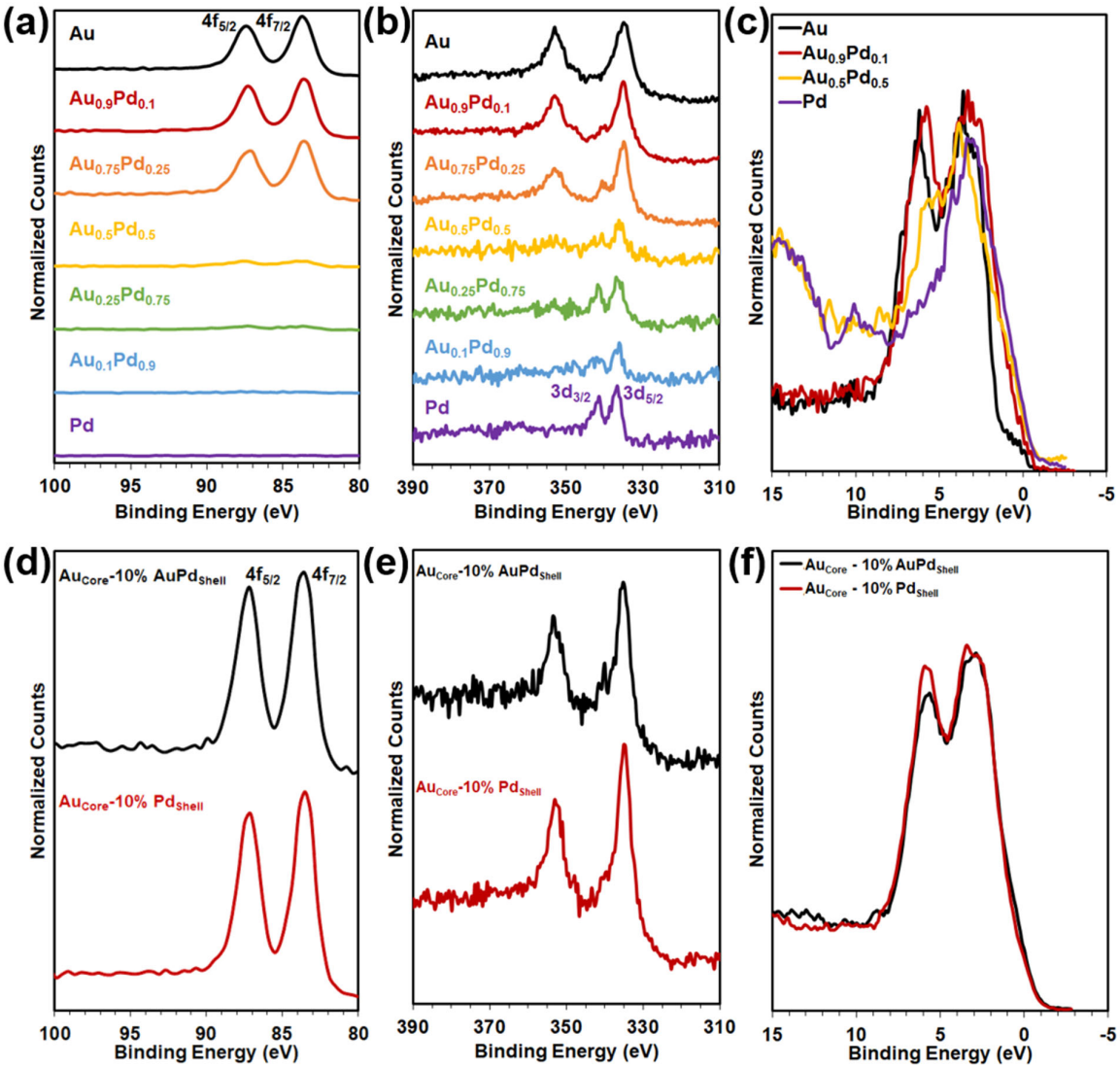

Figure 3. XPS analysis of the (**a**–**c**) $Au_{1-x}Pd_x$ alloys and (**d**–**f**) Au_{Core}–$Au_{1-x}Pd_{x,Shell}$ NPs for the (**a**,**d**) Au 4f, (**b**,**e**) Pd 3d, and (**c**,**f**) VB regions.

Optical properties of $Au_{1-x}Pd_x$ alloy and Au_{Core}–$Au_{1-x}Pd_{x,Shell}$ NPs coupled to the 3.2 eV bandgap semiconductor TiO_2 were characterized by UV–Vis diffuse reflectance spectra (DRS), shown in Figure 4c,d and Supplementary Figure S7. In Figure 4c,d, prepared powders exhibit a red-shifted SPR response compared to the alloys (≥ 50% Au) and core–shell NPs in solution by ~20 and ~15–20 nm, respectively. Interestingly, the plasmonic response was still present on TiO_2 composites but appeared more prominent for the alloy NPs (i.e., ≥ 10% Pd) after coupling to TiO_2, attributed to the dielectric screening interaction of TiO_2 [6]. The λ_{Max} of the alloys on TiO_2 blue-shifted with increasing Pd content, from 547 nm for Au to 450 nm for $Au_{0.1}Pd_{0.9}$. For the core–shell NPs, the λ_{Max} of $AuPd_{Shell}$ red-shifted by ~4 nm in comparison to the Pd_{Shell} owing to the Au in the shell.

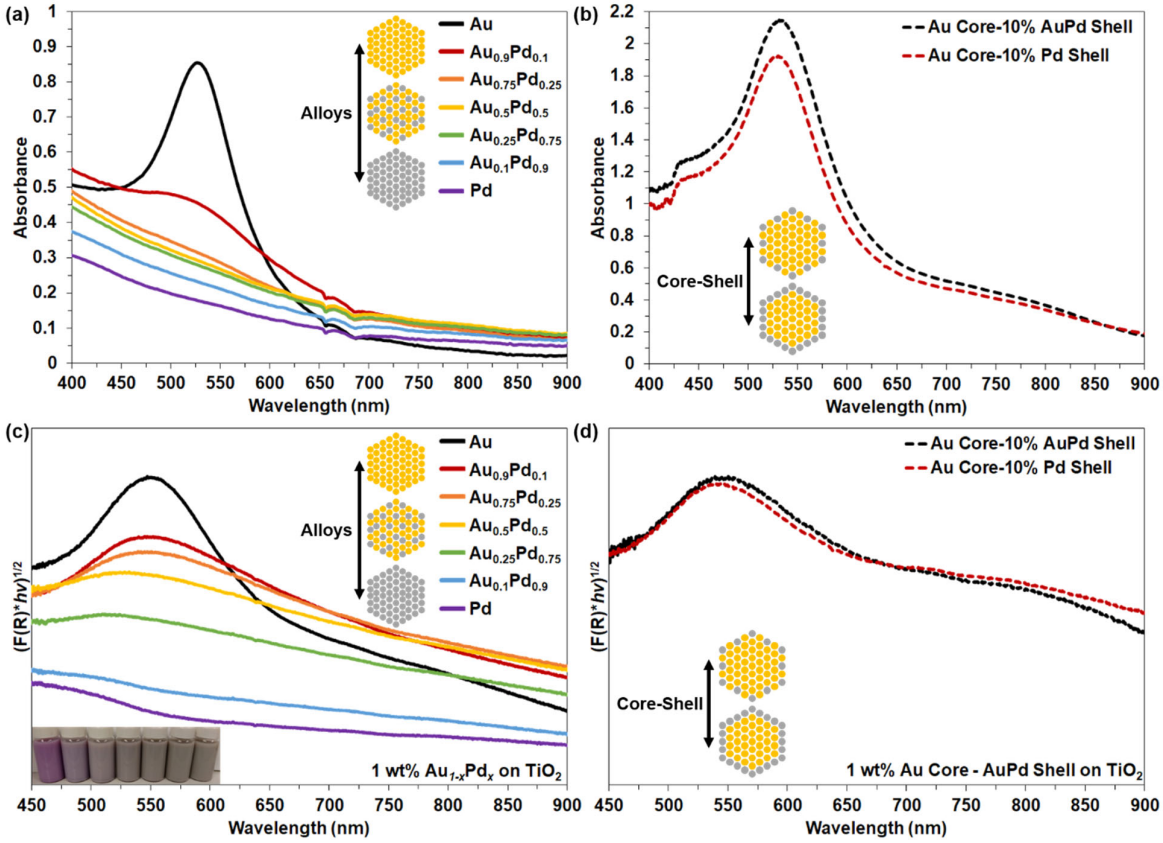

Figure 4. UV–Vis spectra of (**a**) $Au_{1-x}Pd_x$ and (**b**) Au_{Core}–$Au_{1-x}Pd_{x,Shell}$ NPs in solution. UV–Vis DRS of 1 wt.% (**c**) $Au_{1-x}Pd_x$ NPs and (**d**) Au_{Core} NPs with 10% $Au_{0.5}Pd_{0.5,Shell}$ and 10% $Pd_{.Shell}$ on TiO_2 supports, with inset image of $Au_{1-x}Pd_x$ alloy NPs on TiO_2 in a slurry mixture.

DDA was used to model and quantify the plasmonic interactions of metal NPs in physical contact with TiO_2 [6]. Local spatial distributions of the enhanced electric field intensity ($|E/E_0|^2$) and far-field optical spectra of $Au_{1-x}Pd_x$– TiO_2 and Au_{Core}–$Au_{1-x}Pd_{x,Shell}$–TiO_2 heterodimers are shown in Figure 5, as well as Supplementary Table S1 and Figure S8. In each case, the strongest near-field enhancement magnitude is depicted at the heterodimers' calculated resonance wavelength for horizontal polarization (i.e., across x-axis). $Au_{1-x}Pd_x$ NPs were approximated as 10 nm, Au_{Core}–$Au_{1-x}Pd_{x,Shell}$ NPs as 30 nm Au_{Core} with 2 nm shells, and P25 as 25 nm in all cases. Composition was varied based on known dielectric functions for Au and Pd, as well as that previously determined for AuPd [30]. In Figure 5a,b, pure Au NPs exhibited the strongest electric field enhancement followed by AuPd and Pd compositions, which exhibited similar intensities. Therefore, the electric field enhancement should not have a pronounced effect on the photocatalytic activity when comparing AuPd and Pd. However, the ligand effect and other SPR properties (hot-carrier injection and photothermal effects) of AuPd will significantly impact their catalytic activity for EOR compared to monometallic Pd. Au–Pd nanomaterials and TiO_2 exhibit energy localization at the plasmonic metal–semiconductor interfaces via dipole SPR excitations. DDA-simulated absorbance efficiency spectra of the Au–Pd NPs without TiO_2 (Figure 5c) and with TiO_2 (Figure 5d) were in good agreement with the experimentally determined SPR λ_{Max} peak positions shown in Figure 4 and Supplementary Table S1. However, the predicted relative magnitudes for Pd-rich compositions were underestimated, especially with regards to alloy and core–shell NPs in contact with TiO_2. Near-field

maps and simulated absorbance spectra provide qualitative guides for interpreting measured optical influences at AuPd–TiO_2 interfaces for plasmonically driven photocatalytic reactions [6].

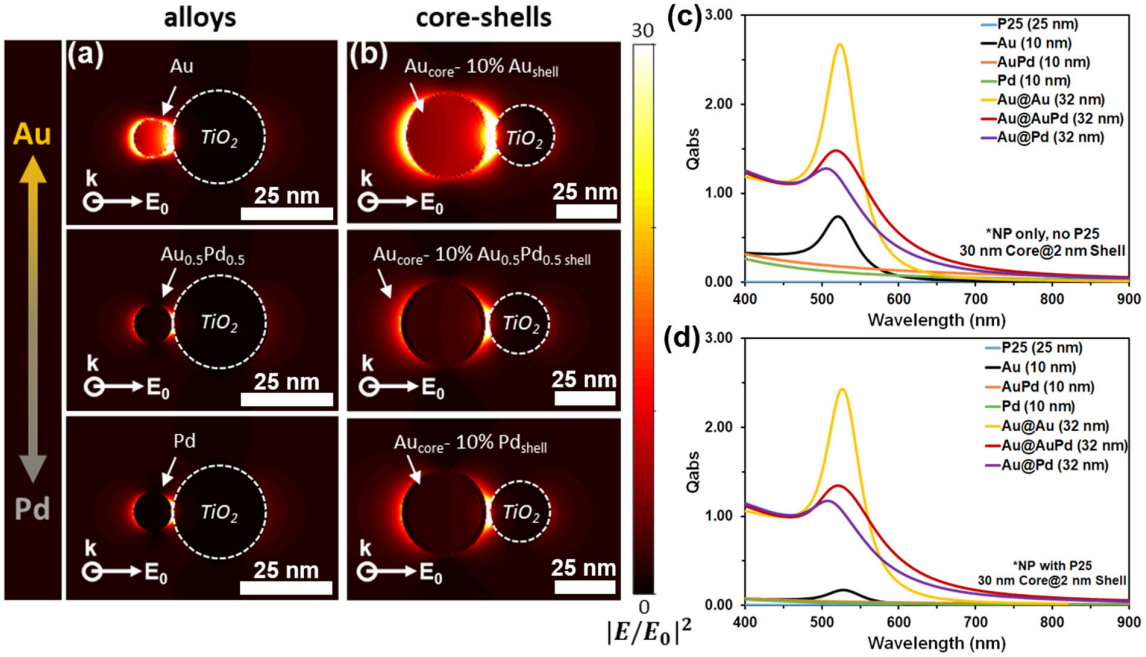

Figure 5. DDA simulations of the spatial distributions of the electric field enhancement ($|E/E_0|^2$) for spherical (**a**) $Au_{1-x}Pd_x$ and (**b**) Au_{Core}–$Au_{1-x}Pd_{x.Shell}$ NPs in contact with a spherical TiO_2 NP under resonance wavelength excitation. Wave vector is incident into the image. DDA simulated absorption efficiency (Q_{abs}) spectra for (**c**) Au–Pd NPs only and (**d**) Au–Pd NPs in contact with TiO_2.

3.2. Photocatalytic Ethanol Oxidation via Au–Pd NPs on TiO_2 Supports

Suspended particle photocatalysis of metal-oxide semiconductors is initiated by the absorption of photons to induce charge separation and diffusion of the photogenerated carriers to surface active sites to react with adsorbed chemical species [3,5,6,46]. Metal-oxide TiO_2 supports were photosensitized with homogeneously alloyed $Au_{1-x}Pd_x$ and heterogeneous Au_{Core}–$Au_{1-x}Pd_{x.Shell}$ NPs to be used as hybrid photoreactors for EtOH photooxidation. Plasmon-mediated photocatalytic EOR performance measurements were conducted under solar-simulated (AM1.5G) irradiation for 1–4 h, while the gaseous oxidation products were measured using a GC-MS-MHE analysis method [5,6]. Thermal background measurements were collected under dark conditions for each sample by heating the photoreactor at 60 °C to thermal equilibrium, which yielded negligible oxidation of EtOH. Plasmonically enhanced photocatalytic mass activities for $Au_{1-x}Pd_x$ and Au_{Core}–$Au_{1-x}Pd_{x.Shell}$ NPs dispersed on TiO_2 are shown in Figure 6, Table 1, and in Supplementary Tables S2 and S3 for the oxidation products of EtOH conversion, acetaldehyde (CH_3CHO, $n = 2e^-$) and carbon dioxide (CO_2, $n = 12e^-$). In Figure 6, the mass activity for CO_2 is plotted on the left axis represented by purple (1 h) and blue (4 h) bars, while the mass activity for CH_3CHO is plotted on the right axis represented by orange diamond (1 h) and green triangle (4 h) markers.

In Figure 6a and Table 1, all of the investigated elemental compositions for the $Au_{1-x}Pd_x$ alloys (outlined in black) and Au_{Core}–$Au_{1-x}Pd_{x.Shell}$ (outlined in red) NPs on TiO_2 were irradiated for 1 h under AM1.5G and the primary photocatalytic products detected by GC-MS-MHE were CO_2 (purple bars) and CH_3CHO (orange diamonds). The activity for TiO_2

without a cocatalyst was 87.11 μmol CO_2/g and 0.60 μmol CH_3CHO/g, as listed in Supplementary Table S2. Mass activity of the $Au_{1-x}Pd_x$ alloys increased with an increase in the Pd content (x = 0 to x = 0.5) from 132.32 μmol CO_2/g and 0.26 μmol CH_3CHO/g for Au to 221.67 μmol CO_2/g and 0.96 μmol CH_3CHO/g for AuPd. However, the mass activity did not significantly increase after increasing the Pd content from x = 0.5 to x = 1, with Pd exhibiting 225.33 μmol CO_2/g and 0.89 μmol CH_3CHO/g. The observed plateau in mass activity for > 50% Pd can be attributed to a loss in the SPR absorption at low Au content. The Au_{Core}-10% AuPd.$_{Shell}$ NPs on TiO_2 exhibited mass activities of 164.99 μmol CO_2/g and 0.36 μmol CH_3CHO/g, which was between that of the alloy compositions of $Au_{0.9}Pd_{0.1}$ (147.09 μmol CO_2/g) and $Au_{0.75}Pd_{0.25}$ (176.76 μmol CO_2/g). In contrast, the Au_{Core}-10% Pd.$_{Shell}$ NPs exhibited the highest mass activity of all samples with 283.28 μmol CO_2/g and 1.06 μmol CH_3CHO/g. The Au core maintains SPR absorption with a thin Pd shell at the surface to enhance catalytic EOR. Coupling plasmonic Au to TiO_2 improves the chemical energy conversion reactions via plasmon-mediated hot electron transfer (PMET)—injection of hot electrons into the CB of a semiconductor. Detailed spectroscopic studies by Tan et al. have proposed the mechanism for photoenhancement due to PMET charge transfer between Au and TiO_2 for EOR: (1) activation of oxygen at oxygen vacancies on TiO_2, (2) dehydrogenation of EtOH to form acetaldehyde, (3) cleaving of C–C bond, (4) further oxidation to form CO_2, and (5) electron transfer from Au to TiO_2 [11,12]. PMET enables Au to accumulate hot holes and stabilize the Pd as a cocatalyst; facilitating the Au–Pd NPs to act as the primary active site for EOR [3,6]. Plasmon-induced heating (photothermal) provides the means to overcome the thermal barrier necessary to selectively cleave the C–C bond and hinder the poisoning effects on Pd [5,6,9]. Addition of Au–Pd cocatalysts with either an alloy or core–shell nanostructure resulted in an increase in the CO_2 mass activity, i.e., the complete conversion of EtOH.

Table 1. Mass activity of 1 wt.% $Au_{1-x}Pd_x$ and Au_{Core}–$Au_{1-x}Pd_{x.Shell}$ NPs on TiO_2 supports under AM1.5G irradiation for 1 h determined from GC-MS-MHE analysis.

Sample	μmol CO_2/g	μmol CH_3CHO/g
TiO_2	87.11	0.60
Au	132.32	0.26
$Au_{0.9}Pd_{0.1}$	147.09	0.37
$Au_{0.75}Pd_{0.25}$	176.76	0.63
$Au_{0.5}Pd_{0.5}$	221.67	0.96
$Au_{0.25}Pd_{0.75}$	226.43	0.92
$Au_{0.1}Pd_{0.9}$	228.62	0.84
Pd	225.33	0.89
Au-10% AuPd	164.99	0.36
Au-10% Pd	283.28	1.06

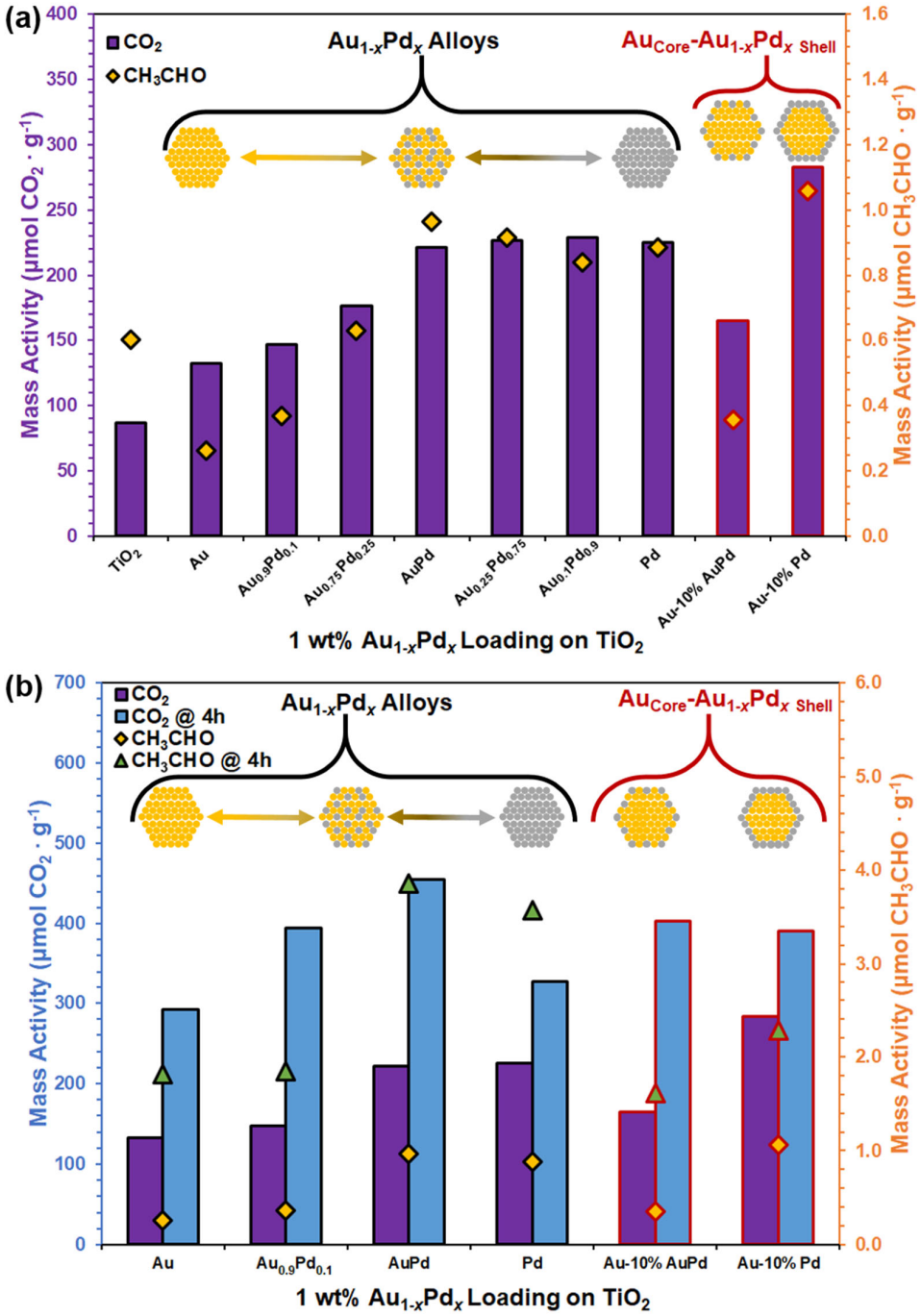

Figure 6. Plasmonically enhanced photo-oxidation of EtOH to CO_2 and/or CH_3CHO intermediary for 1 h duration for $Au_{1-x}Pd_x$ alloy (outlined in black) and Au_{Core}–$Au_{1-x}Pd_{x,Shell}$ (outlined in red) NPs on TiO_2 under (**a**) AM1.5G irradiation for all compositions and (**b**) 1–4 h AM1.5G irradiation for select compositions. Note: CO_2 is plotted on the left axis represented by purple (1 h) and blue (4 h) bars, while CH_3CHO is plotted on the right axis represented by orange diamond (1 h) and green triangle (4 h) markers.

In Figure 6b, Au, $Au_{0.9}Pd_{0.1}$, AuPd, Pd, Au_{Core}-10% AuPd.$_{Shell}$, and Au_{Core}–10% Pd.$_{Shell}$ NPs on TiO_2 were further investigated as photocatalysts by comparing product yields under prolonged (4 h) irradiation, listed in Table 2 and Supplementary Table S3. After 4 h irradiation, the yield of CO_2 (blue bars) and CH_3CHO (green triangles) increased for all

compositions in comparison to the yields collected after 1 h irradiation (CO_2, purple bars; CH_3CHO, orange diamonds). Pd had the lowest EOR activity for complete EtOH conversion of the Pd-containing cocatalysts (328 μmol CO_2/g). Initial rate of conversion for Pd diminished by 64% to 82 μmol $CO_2 \cdot g^{-1} \cdot h^{-1}$ after 4 h irradiation owing to binding of intermediates to its surface active sites [5,25,30]. Plasmonic Au cocatalysts exhibited the lowest overall activity of the cocatalysts after prolonged irradiation (292 CO_2/g), with its initial rate of conversion diminished by 45% to 73.09 μmol $CO_2 \cdot g^{-1} \cdot h^{-1}$. Notably, the product yields for $Au_{1-x}Pd_x$ alloy and $Au_{Core}–Au_{1-x}Pd_{x.Shell}$ compositions that contained ~5–10 mol% Pd (i.e., $Au_{0.9}Pd_{0.1}$, Au-10% AuPd, and Au-10% Pd) were relatively similar with regard to complete EtOH conversion (391–403 CO_2/g). The rate of complete EtOH conversion (97.68–100.78 μmol $CO_2 \cdot g^{-1} \cdot h^{-1}$) indicated similar reactivity and stability for alloy and core–shell NPs after prolonged irradiation. Therefore, nanostructuring (alloy vs. core–shell) at low Pd content (≤10% Pd) did not have a pronounced effect on the mass activity for long duration photocatalytic measurements. AuPd (1:1 mole ratio) alloy on TiO_2 was the most active for complete EtOH conversion after prolonged AM1.5G irradiation (456 μmol CO_2/g) and retained 67% of its initial rate of conversion (113.92 μmol $CO_2 \cdot g^{-1} \cdot h^{-1}$). Alloyed NPs can exhibit plasmonic, catalytic, and ligand effects observed in core–shell NPs, with the addition of the atomically distributed surface active sites to inhibit side reactions and poisoning [18,30,47]. The AuPd alloy exhibited SPR absorption and contained a sufficient amount of Pd metal to significantly improve its reactant chemisorption and subsequent EOR activity. Catalytic Pd enabled the retention and utilization of photogenerated carriers generated in Au for photocatalytic EOR.

Table 2. Mass activities of 1 wt.% $Au_{1-x}Pd_x$ and $Au_{Core}–Au_{1-x}Pd_{x.Shell}$ NPs for select compositions on TiO_2 supports under AM1.5G for 4 h, determined from GC-MS-MHE analysis.

Sample	Total μmol CO_2/g	Total μmol CH_3CHO/g	Total Rate (μmol $CO_2 \cdot g^{-1} \cdot h^{-1}$)	Total Rate (μmol $CH_3CHO \cdot g^{-1} \cdot h^{-1}$)
Au	292.35	1.82	73.09	0.45
$Au_{0.9}Pd_{0.1}$	394.63	1.84	98.66	0.46
$Au_{0.5}Pd_{0.5}$	455.67	3.86	113.92	0.96
Pd	327.98	3.57	82.00	0.89
Au-10% AuPd	403.13	1.61	100.78	0.40
Au-10% Pd	390.72	2.28	97.68	0.57

3.3. Electrochemical Ethanol Oxidation via Au–Pd NPs on Carbon Supports

Photocatalytically active $Au_{1-x}Pd_x$ alloys and $Au_{Core}–Au_{1-x}Pd_{x.Shell}$ NPs were selected for electrochemical measurement of their EOR performance. Figure 7 shows cyclic voltammetry (CV) scans of $Au_{1-x}Pd_x$ and $Au_{Core}–Au_{1-x}Pd_{x.Shell}$ NPs on conductive carbon supports on a rotating disk electrode (RDE) immersed in 0.5 M EtOH (1 M KOH supporting electrolyte, 25 °C) under dark conditions. Onset potentials were identified as the threshold voltage for appreciable positive current, which indicated the start of the electrochemically driven EOR. Onset potentials during the anodic forward scan (i.e., left to right; V_F and I_F) were found to be reductively shifted from +0.72 V for Au to +0.30 V for Pd, listed in Table 3. Previous studies have reported ~1.25 to 5 mA/cm^2 for pure Au to Pd compositions, respectively [48,49]. Greater overpotential on Au is characteristic of EOR on Au compared with Pd for bulk metal surfaces [25,30,33]. The EOR current peaks for both samples during their anodic scan (V_F and I_F) were characteristically followed by a decrease in current owing to surface passivation of the active catalytic sites that were covered by EOR intermediate products [25,30,33]. Active sites were cleaned upon the reverse, cathodic scans (i.e., right to left; V_R and I_R), which resulted in the positive-current takeoff to higher EOR peak current magnitude owing to the freshly renewed catalytic surface [30]. Supplementary Figure S9 compares CVs in the dark immersed in 1 M KOH supporting electrolyte without

0.5 M EtOH. Peak anodic EOR current for the $Au_{1-x}Pd_x$ alloys increased from 1.51 mA cm^{-2} for Au, 9.26 mA cm^{-2} for $Au_{0.9}Pd_{0.1}$, 29.14 mA cm^{-2} for AuPd, and to 30.80 mA cm^{-2} for Pd, with current densities comparable or better than previous studies [48–52]. AuPd alloy exhibited similar electrochemical EOR activity as pure Pd despite 50% less Pd content. Increased EOR activity for the AuPd alloy is in part due to the superior catalytic performance inherent to Pd, as well as the resistance to catalyst poisoning inherent to Au. No significant changes in the onset potential or current density were observed for > 50% Pd alloy composition. In contrast, peak anodic current densities of the core–shell NPs in Figure 7b were lower and anodically shifted to higher onset potentials with 3.37 mA cm^{-2} at 0.82 V for Au_{Core}–$AuPd._{Shell}$ and 1.55 mA cm^{-2} at 0.94 V for Au_{Core}–$Pd._{Shell}$. Secondary anodic peaks at higher potential were attributed to the Au signature for the $Au_{0.9}Pd_{0.1}$ alloy with 3.81 mA cm^{-2} at 1.17 V, Au_{Core}–$AuPd._{Shell}$ with 1.60 mA cm^{-2} at 1.18 V, and Au_{Core}–$Pd._{Shell}$ with 2.96 mA cm^{-2} at 1.21 V. Under dark conditions, electrochemical properties were investigated for alloy and core–shell NPs on conductive carbon supports without SPR effects. Homogenous mixing of Au and Pd yielded optimal results, while heterogeneous core–shells separated the metals into defined regions, resulting in lower current densities at analogous compositions.

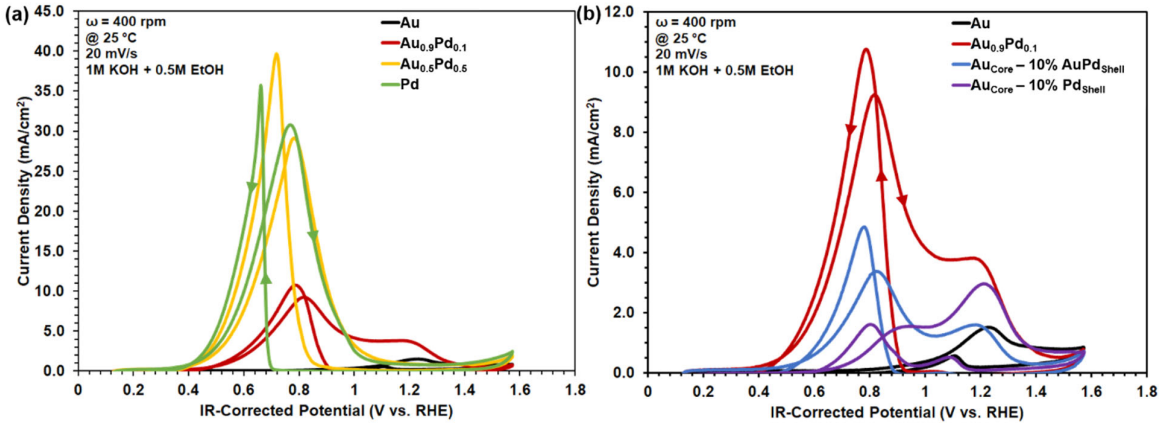

Figure 7. Electrochemical CVs for EtOH oxidation catalyzed by 20 wt.% (**a**) $Au_{1-x}Pd_x$ and (**b**) Au_{Core}–$Au_{1-x}Pd_{x.Shell}$ NPs dispersed on carbon supports deposited onto a rotating disk, glassy carbon working electrode. Reference and counter electrodes were Ag/AgCl and a Pt coil, respectively, immersed in 0.5 M EtOH with 1 M KOH supporting electrolyte.

Table 3. Electrochemical onset potentials, peak potentials, and peak current densities for forward and reverse CV scans of the $Au_{1-x}Pd_x$ and Au_{Core}–$Au_{1-x}Pd_{x.Shell}$ NPs on carbon supports in the dark.

Composition	Onset (V)	V_F (V)	I_F (mA/cm²)	V_R (V)	I_R (mA/cm²)
Au	0.72	1.23	1.51	1.10	0.56
$Au_{0.9}Pd_{0.1}$	0.35	0.82	9.26	0.79	10.75
		1.17	3.81	1.03	0.04
AuPd	0.32	0.79	29.14	0.66	35.74
Pd	0.30	0.77	30.80	0.66	35.74
Au-10% AuPd	0.40	0.82	3.37	0.78	4.85
		1.18	1.60		
Au-10% Pd	0.52	0.94	1.55	0.80	1.61
		1.21	2.96	1.08	0.52

3.4. Photoelectrochemical Ethanol Oxidation via Au–Pd NPs on TiO_2 Supports

The selected $Au_{1-x}Pd_x$ alloys and Au_{Core}–$Au_{1-x}Pd_{x.Shell}$ NPs were further investigated by CV and chronoamperometry (CA) for their SPR-induced photoelectrochemical (PEC)

EOR by photosensitizing TiO_2 supports. CV scans in the dark and under AM1.5G irradiation are shown in Supplementary Figures S10–S12. Catalytic metals like Pt and Pd enhance the extraction and use of plasmonic carriers generated in Au [4,18,20,28,29,43,53,54]. Furthermore, hot electron transfer and photothermal processes can facilitate intermediate removal during irradiation [3,5,9]. Elucidation of the role of SPR effects on EOR motivated solar-simulated CA photocurrent studies. Plasmon-enhanced EOR photocurrents were measured via CA scans on a RDE immersed in 0.5 M EtOH (1 M KOH supporting electrolyte, 25 °C) for current density (Figure 8a) and mass activity (Figure 8b) measurements. CA measurements were held at a bias of appreciable current (+0.72 V vs. RHE), with 250 s on/off chopping of broadband AM1.5G irradiation. Applied potential improves electron transport to the back contact and decreases the surface recombination rate, while demonstrating appreciable EOR current for both alloy and core–shell compositions of interest. Analyses focus on the average photocurrent magnitude measured during the first "light on" step and after 1900 s chopped irradiance, as shown in Figure 8 and in Supplementary Tables S4 and S5.

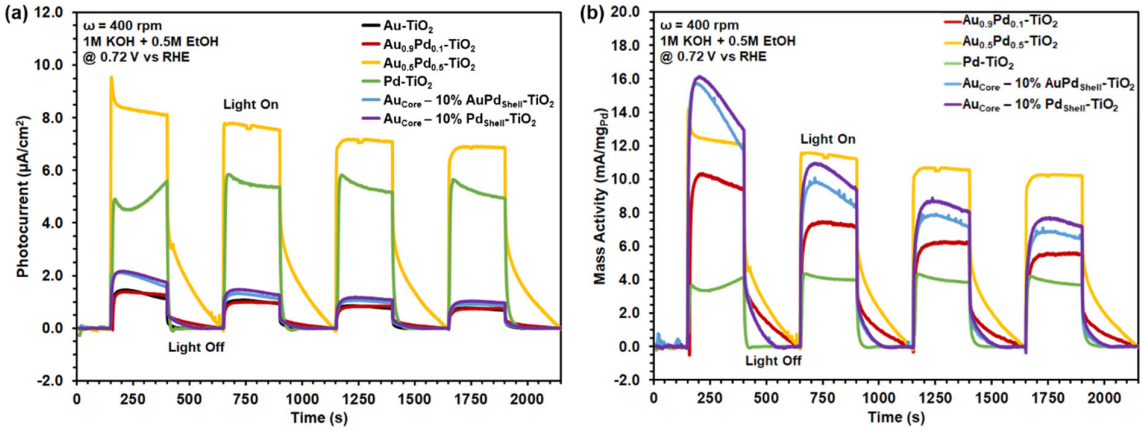

Figure 8. Photoelectrochemical chronoamperometry for EtOH oxidation catalyzed by 1 wt.% $Au_{1-x}Pd_x$ and Au_{Core}–$Au_{1-x}Pd_{x.Shell}$ NPs dispersed on TiO_2 deposited onto a rotating disk, glassy carbon working electrode. Reference and counter electrodes were Ag/AgCl and a Pt coil, respectively, immersed in 0.5 M EtOH with 1 M KOH supporting electrolyte. Photo-induced (**a**) current densities and (**b**) mass activities held at +0.72 V (vs. RHE) under 250 s on/off chopping of solar-simulated AM1.5G irradiation. The baseline (i.e., 0 μA cm^{-2}) is the dark current.

Immediate photocurrent response resulted from the separation of photogenerated electron–hole pairs at the electrode–electrolyte interface. Anodic (positive) spikes in photocurrent indicated accumulation of charge at the electrode–electrolyte interface, while cathodic (negative) transients are indicative of charge recombination. Lack of photocurrent transients indicated unimpeded charge transfer from the electrode to the electrolyte, thereby hole transfer was facilitated at the catalyst surface for EOR [55–57]. Average peak EOR photocurrent densities generated under AM1.5G irradiation on TiO_2 in Figure 8a were 1.31 μA cm^{-2} for Au, 1.31 μA cm^{-2} for $Au_{0.9}Pd_{0.1}$, 1.43 μA cm^{-2} for Au_{Core}–$AuPd_{Shell}$, and 1.97 μA cm^{-2} for Au_{Core}–Pd_{Shell}. Notably, no photo-induced current enhancement was observed for Au–Pd alloy thin films absent of SPR effects in our previous studies [30]. Au–Pd photosensitized samples were reactivated by successive CV scans to remove surface-adsorbed intermediates. Au-rich compositions (Au, $Au_{0.9}Pd_{0.1}$, Au_{Core}-$AuPd_{Shell}$, Au_{Core}–Pd_{Shell}) act as hole accumulation sites, creating a positively charged surface to promote the adsorption of electron donors such as EtOH [11,12]. However, interband transitions that occur at shorter wavelengths ($\lambda < 600$ nm) between filled *d*-band and empty *sp*-states dominate for Au-rich NP compositions, resulting primarily in $2e^-$ products rather than complete oxidation [6,11,12]. Appreciable loss in photocurrent during sustained bias holds was observed overtime for all Au–Pd photosensitized samples with photocurrent retention of 47% for Au, 53% for $Au_{0.9}Pd_{0.1}$, 40% for Au_{Core}–$AuPd_{Shell}$, and 44% for Au_{Core}–Pd_{Shell}

on TiO_2 after 1900 s at the sustained bias (0.72 V vs. RHE). Relatively low photocurrents for Au-rich compositions suggest that some excited carriers on the cocatalysts relax via electron–phonon scattering, thereby increasing the surface temperature. While photothermal heating can contribute to photocatalytic activity and gaseous product yields (Figure 6), higher rates of hot-carrier separation and transfer in Au-rich compositions are necessary for increased photocurrents (Figure 8).

Alloying ≥ 50% Pd with Au had the largest impact on the EOR photocurrent, with a photocurrent density of 8.32 μA cm^{-2} for AuPd alloy on TiO_2. Notably, AuPd alloy on TiO_2 retained 72% of its initial photocurrent after 1900 s at the sustained bias. Alloying Au with Pd resulted in an even distribution of metal active sites for reactant binding; reducing the stability of the intermediate and improving activity [58]. The increase in photocurrent was attributed to interband excitations that initiated injection of *d*-band holes from the Au into the Pd active sites for subsequent reaction with adsorbed species [59]. Slow relaxation of the photocurrent after the "light on" step for AuPd alloy indicated accumulation of holes at the electrode–electrolyte interface, facilitated favorable reaction kinetics, and hindered charge recombination [55–57]. In comparison, catalytic Pd on TiO_2 generated 4.74 μA cm^{-2} and retained 84% of its initial photocurrent after 1900 s owing to Pd acting as a hole scavenger, which improved charge separation at the metal–semiconductor interface. Average photo-enhancement in terms of mass activity (mA/mg_{Pd}) in Figure 8b showed a moderate improvement for core–shell NPs (10.60–14.70 mA/mg_{Pd}) in comparison to the analogous alloy composition of $Au_{0.9}Pd_{0.1}$ (9.76 mA/mg_{Pd}). Photocurrent enhancements were observed for all bimetallic Au–Pd compositions (9.76–14.70 mA/mg_{Pd}) compared to pure Pd (3.53 mA/mg_{Pd}). Initially, core–shell NPs exhibited high mass activity performance at the first "light on" step but rapidly decayed. AuPd (1:1 mole ratio) alloy retained the highest mass activity (10.20 mA/mg_{Pd}) after 1900 s compared to all measured compositions and nanostructured catalysts. Bimetallic AuPd alloy catalysts exhibited the ability to selectively drive photochemical and PEC reactions at improved efficiency with the assistance of their SPR and ligand effects.

4. Conclusions

Bimetallic Au–Pd NPs were synthetically modified to influence the plasmonic near-field enhancement, optical absorption, and catalytic activity resultant from PMET and photothermal effects. TEM imaging and elemental analysis confirmed the composition and nanostructuring (alloy vs. core–shell). XPS revealed a shift in *d*-band onset toward the E_F and an increase in the DOS at the E_F with an increase in Pd content. Modifying the Au–Pd composition provides atomic control over tuning the ligand effect to impact reactant adsorption to the catalyst surface, and thereby the catalytic activity. UV–vis spectroscopy revealed the plasmonic response was retained and appreciable for alloys containing ≥ 50% Au and core–shell nanostructures with intact plasmonic Au cores. Au–Pd alloys and core–shells exhibited E_F below the CB of TiO_2, as confirmed by XPS, and the composites maintained their SPR effect that progressively blue-shifted with increasing Pd, as confirmed by UV–Vis DRS. DDA simulations of the spatial distributions of the electric field enhancement showed pure Au exhibited the strongest SPR response, with AuPd and Pd exhibiting similar intensity responses, localized at the metal–semiconductor interface. Photocatalytic and electrochemical oxidation of EtOH to CO_2 under dark and solar-simulated irradiation was studied, with a focus on product selectivity, C–C bond breaking, and mitigating catalyst poisoning. Supported AuPd (1:1 mole ratio) alloy yielded optimal photocatalytic (456 μmol CO_2/g), electrochemical (29.14 mA·cm^{-2}), and PEC (8.32 μA cm^{-2}) results owing to metallic effects (plasmonic, catalytic, ligand effects) and atomically distributed Au and Pd surface active sites to inhibit side reactions and poisoning. The AuPd alloy was found to be the ideal composition and nanostructured bimetallic for complete EtOH conversion. Photogenerated holes drive the photo-oxidation of EtOH primarily on the AuPd alloy and photothermal effects improve intermediate desorption from the catalyst surface, provid-

ing a method to selectively cleave C–C bonds. Plasmonic bimetallic nanostructures provide a pathway for driving desired photocatalytic and PEC reactions with superior catalytic activity and selectivity.

Supplementary Materials: The following are available online at www.mdpi.com/2073-4352/11/3/226/s1, Figure S1 and S2: EDXS, Figure S3: XPS survey scans, Figure S4: XPS scans of the VB region, Figure S5 and S6: UV-Vis extinction spectra, Figure S7: UV-Vis DRS, Figure S8: DDA simulated absorption spectra, Figure S9 and S10: Electrochemical CVs in 1 M KOH, Figure S11 and S12: Electrochemical CVs of EtOH oxidation, Table S1: Experimental and DDA calculated SPR peaks, Tables S2 and S3: Photocatalytic mass activities, Table S4: Photo-induced current densities, Table S5: Photo-induced mass activities.

Author Contributions: Conceptualization, methodology, investigation, writing—original draft preparation, J.B.; electron microscopy, A.C.L.; numerical computation, G.T.F.; X-ray photoelectron spectroscopy, D.R.B.; writing—review and editing, J.B., A.C.L., G.T.F., and D.R.B.; supervision, D.R.B. All authors have read and agreed to the published version of the manuscript.

Funding: This work was sponsored by DEVCOM-Army Research Laboratory.

Data Availability Statement: Data is contained within the article or supplementary material.

Acknowledgments: The views and conclusions contained in this document are those of the authors and should not be interpreted as representing official policies, either expressed or implied, of the DEVCOM-Army Research Laboratory or the U.S. Government. The U.S. Government is authorized to reproduce and distribute reprints for government purposes notwithstanding any copyright notation herein.

Conflicts of Interest: The authors declare no conflict of interest.

Abbreviations

Au, gold; Pd, palladium; NPs, nanoparticles; SPR, surface plasmon resonance; EtOH, ethanol; EOR, ethanol oxidation reaction; C–C, carbon–carbon bond; PEC, photoelectrochemistry; DDA, discrete dipole approximation; UV-Vis, ultraviolet-visible; NIR, near-infrared; XPS, X-ray photoelectron spectroscopy; EDXS, energy-dispersive X-ray spectroscopy; HAADF-STEM, high-angle annular dark-field imaging scanning transmission electron microscopy; STEM, scanning transmission electron microscopy; TEM, transmission electron microscopy; GC-MS-MHE, gas chromatography–mass spectrometry–multiple headspace extraction; RDE, rotating disk electrode; RHE, reversible hydrogen electrode; CV, cyclic voltammetry; CA, chronoamperometry; VB, valence band; CB, conduction band; DOS, density of states; DFT, density functional theory; PMET, plasmon-mediated hot electron transfer.

References

1. Wang, M.; Ma, J.; Liu, H.; Luo, N.; Zhao, Z.; Wang, F. Sustainable Productions of Organic Acids and Their Derivatives from Biomass via Selective Oxidative Cleavage of C–C Bond. *ACS Catal.* **2018**, *8*, 2129–2165.
2. Lamy, C.; Belgsir, E.M.; Léger, J.M. Electrocatalytic Oxidation of Aliphatic Alcohols: Application to the Direct Alcohol Fuel Cell (DAFC). *J. Appl. Electrochem.* **2001**, *31*, 799–809.
3. Zhang, Y.; He, S.; Guo, W.; Hu, Y.; Huang, J.; Mulcahy, J.R.; Wei, W.D. Surface-Plasmon-Driven Hot Electron Photochemistry. *Chem. Rev.* **2018**, *118*, 2927–2954.
4. Ortiz, N.; Zoellner, B.; Hong, S.J.; Ji, Y.; Wang, T.; Liu, Y.; Maggard, P.A.; Wang, G. Harnessing Hot Electrons from Near IR Light for Hydrogen Production Using Pt-End-Capped-AuNRs. *ACS Appl. Mater. Interfaces* **2017**, *9*, 25962–25969.
5. Boltersdorf, J.; Leff, A.C.; Forcherio, G.T.; McClure, J.P.; Lundgren, C.A. Surface Plasmon Resonant Gold-Palladium Bimetallic Nanoparticles for Promoting Catalytic Oxidation. *MRS Adv.* **2019**, *4*, 1877–1886.
6. Boltersdorf, J.; Forcherio, G.T.; McClure, J.P.; Baker, D.R.; Leff, A.C.; Lundgren, C. Visible Light-Promoted Plasmon Resonance to Induce "Hot" Hole Transfer and Photothermal Conversion for Catalytic Oxidation. *J. Phys. Chem. C* **2018**, *122*, 28934–28948.
7. McClure, J.P.; Grew, K.N.; Baker, D.R.; Gobrogge, E.; Das, N.; Chu, D. Harvesting Resonantly-Trapped Light for Small Molecule Oxidation Reactions at the Au/α-Fe_2O_3 Interface. *Nanoscale* **2018**, *10*, 7833–7850.
8. Jain, P.K. Taking the Heat off of Plasmonic Chemistry. *J. Phys. Chem. C* **2019**, *123*, 24347–24351.
9. Qiu, J.; Wei, W.D. Surface Plasmon-Mediated Photothermal Chemistry. *J. Phys. Chem. C* **2014**, *118*, 20735–20749.

10. Kim, S.M.; Lee, S.W.; Moon, S.Y.; Park, J.Y. The Effect of Hot Electrons and Surface Plasmons on Heterogeneous Catalysis. *J. Phys. Condens. Matter* **2016**, *28*, 254002.
11. Tan, T.H.; Scott, J.; Ng, Y.H.; Taylor, R.A.; Aguey-Zinsou, K.F.; Amal, R. Understanding Plasmon and Band Gap Photoexcitation Effects on the Thermal-Catalytic Oxidation of Ethanol by TiO_2-Supported Gold. *ACS Catal.* **2016**, *6*, 1870–1879.
12. Tan, T.H.; Scott, J.; Ng, Y.H.; Taylor, R.A.; Aguey-Zinsou, K.F.; Amal, R. C-C Cleavage by Au/TiO_2 during Ethanol Oxidation: Understanding Bandgap Photoexcitation and Plasmonically Mediated Charge Transfer via Quantitative in Situ DRIFTS. *ACS Catal.* **2016**, *6*, 8021–8029.
13. Li, K.; Hogan, N.J.; Kale, M.J.; Halas, N.J.; Nordlander, P.; Christopher, P. Balancing Near-Field Enhancement, Absorption, and Scattering for Effective Antenna-Reactor Plasmonic Photocatalysis. *Nano Lett.* **2017**, *17*, 3710–3717.
14. Kumar, P. V.; Norris, D.J. Tailoring Energy Transfer from Hot Electrons to Adsorbate Vibrations for Plasmon-Enhanced Catalysis. *ACS Catal.* **2017**, *7*, 8343–8350.
15. Jovic, V.; Chen, W.-T.; Sun-Waterhouse, D.; Blackford, M.G.; Idriss, H.; Waterhouse, G.I.N. Effect of Gold Loading and TiO_2 Support Composition on the Activity of Au/TiO_2 Photocatalysts for H_2 Production from Ethanol–Water Mixtures. *J. Catal.* **2013**, *305*, 307–317.
16. Guo, J.; Zhang, Y.; Shi, L.; Zhu, Y.; Mideksa, M.F.; Hou, K.; Zhao, W.; Wang, D.; Zhao, M.; Zhang, X.; et al. Boosting Hot Electrons in Hetero-Superstructures for Plasmon-Enhanced Catalysis. *J. Am. Chem. Soc.* **2017**, *139*, 17964–17972.
17. Joplin, A.; Hosseini Jebeli, S.A.; Sung, E.; Diemler, N.; Straney, P.J.; Yorulmaz, M.; Chang, W.S.; Millstone, J.E.; Link, S. Correlated Absorption and Scattering Spectroscopy of Individual Platinum-Decorated Gold Nanorods Reveals Strong Excitation Enhancement in the Nonplasmonic Metal. *ACS Nano* **2017**, *11*, 12346–12357.
18. Sytwu, K.; Vadai, M.; Dionne, J.A. Bimetallic Nanostructures: Combining Plasmonic and Catalytic Metals for Photocatalysis. *Adv. Phys. X* **2019**, *4*, 389-422.
19. Zheng, Z.; Xie, W.; Li, M.; Ng, Y.H.; Wang, D.W.; Dai, Y.; Huang, B.; Amal, R. Platinum Electrocatalysts with Plasmonic Nano-Cores for Photo-Enhanced Oxygen-Reduction. *Nano Energy* **2017**, *41*, 233–242.
20. Zheng, Z.; Tachikawa, T.; Majima, T. Plasmon-Enhanced Formic Acid Dehydrogenation Using Anisotropic Pd-Au Nanorods Studied at the Single-Particle Level. *J. Am. Chem. Soc.* **2015**, *137*, 948–957.
21. Zheng, Z.; Tachikawa, T.; Majima, T. Single-Particle Study of Pt-Modified Au Nanorods for Plasmon-Enhanced Hydrogen Generation in Visible to near-Infrared Region. *J. Am. Chem. Soc.* **2014**, *136*, 6870–6873.
22. Koelling, D.; Freeman, A.; Mueller, F.; Johnson, P.B.; Christy, R.W. Optical Constants of the Noble Metals. *Phys. Rev. B* **1963**, *11*, 1318–245.
23. Olson, J.; Dominguez-Medina, S.; Hoggard, A.; Wang, L.Y.; Chang, W.S.; Link, S. Optical Characterization of Single Plasmonic Nanoparticles. *Chem. Soc. Rev.* **2015**, *44*, 40–57.
24. Hartland, G. V. Optical Studies of Dynamics in Noble Metal Nanostructures. *Chem. Rev.* **2011**, *111*, 3858–3887.
25. Liang, Z.X.; Zhao, T.S.; Xu, J.B.; Zhu, L.D. Mechanism Study of the Ethanol Oxidation Reaction on Palladium in Alkaline Media. *Electrochim. Acta* **2009**, *54*, 2203–2208.
26. Fan, F.R.; Liu, D.Y.; Wu, Y.F.; Duan, S.; Xie, Z.X.; Jiang, Z.Y.; Tian, Z.Q. Epitaxial Growth of Heterogeneous Metal Nanocrystals: From Gold Nano-Octahedra to Palladium and Silver Nanocubes. *J. Am. Chem. Soc.* **2008**, *130*, 6949–6951.
27. Dejarnette, D.; Roper, D.K. Electron Energy Loss Spectroscopy of Gold Nanoparticles on Graphene. *J. Appl. Phys.* **2014**, *116*, 054313.
28. Forcherio, G.T.; Baker, D.R.; Leff, A.C.; Boltersdorf, J.; McClure, J.P.; Grew, K.N.; Lundgren, C.A. Photodeposition of Pd onto Colloidal Au Nanorods by Surface Plasmon Excitation. *J. Vis. Exp.* **2019**, *2019*, 6–11.
29. Forcherio, G.T.; Baker, D.R.; Boltersdorf, J.; Leff, A.C.; McClure, J.P.; Grew, K.N.; Lundgren, C.A. Targeted Deposition of Platinum onto Gold Nanorods by Plasmonic Hot Electrons. *J. Phys. Chem. C* **2018**, *122*, 28901–28909.
30. McClure, J.P.; Boltersdorf, J.; Baker, D.R.; Farinha, T.G.; Dzuricky, N.; Villegas, C.E.P.; Rocha, A.R.; Leite, M.S. Structure-Property-Performance Relationship of Ultrathin Pd-Au Alloy Catalyst Layers for Low-Temperature Ethanol Oxidation in Alkaline Media. *ACS Appl. Mater. Interfaces* **2019**, *11*, 24919–24932.
31. Monyoncho, E.A.; Steinmann, S.N.; Michel, C.; Baranova, E.A.; Woo, T.K.; Sautet, P. Ethanol Electro-Oxidation on Palladium Revisited Using Polarization Modulation Infrared Reflection Absorption Spectroscopy (PM-IRRAS) and Density Functional Theory (DFT): Why Is It Difficult to Break the C-C Bond? *ACS Catal.* **2016**, *6*, 4894–4906.
32. Lai, S.C.S.; Kleijn, S.E.F.; Öztürk, F.T.Z.; Van Rees Vellinga, V.C.; Koning, J.; Rodriguez, P.; Koper, M.T.M. Effects of Electrolyte PH and Composition on the Ethanol Electro-Oxidation Reaction. *Catal. Today* **2010**, *154*, 92–104.
33. Kwon, Y.; Lai, S.C.S.; Rodriguez, P.; Koper, M.T.M. Electrocatalytic Oxidation of Alcohols on Gold in Alkaline Media: Base or Gold Catalysis? *J. Am. Chem. Soc.* **2011**, *133*, 6914–6917.
34. Wang, Y.; Zou, S.; Cai, W. Bin Recent Advances on Electro-Oxidation of Ethanol on Pt- and Pd-Based Catalysts: From Reaction Mechanisms to Catalytic Materials. *Catalysts* **2015**, *5*, 1507–1534.
35. Kadkhodazadeh, S.; Anggoro Ardy Nugroho, F.; Langhammer, C.; Beleggia, M.; B. Wagner, J. Optical Property–Composition Correlation in Noble Metal Alloy Nanoparticles Studied with EELS. *ACS Photonics* **2019**, *6*, 779–786.
36. Hoggard, A.; Wang, L.Y.; Ma, L.; Fang, Y.; You, G.; Olson, J.; Liu, Z.; Chang, W.S.; Ajayan, P.M.; Link, S. Using the Plasmon Linewidth to Calculate the Time and Efficiency of Electron Transfer between Gold Nanorods and Graphene. *ACS Nano* **2013**, *7*, 11209–11217.
37. Draine, B.T.; Flatau, P.J. Discrete-Dipole Approximation for Scattering Calculations. *J. Opt. Soc. Am. A* **1994**, *11*, 1491–1499.

38. Flatau, P.J.; Draine, B.T. Fast near Field Calculations in the Discrete Dipole Approximation for Regular Rectilinear Grids. *Opt. Express* **2012**, *20*, 1247–1252.
39. Draine, B.T.; Flatau, P.J. Discrete-Dipole Approximation for Periodic Targets: Theory and Tests. *J. Opt. Soc. Am. A* **2008**, *25*, 2693.
40. Forcherio, G.T.; Boltersdorf, J.; McClure, J.P.; Leff, A.C.; Baker, D.R.; Lundgren, C.A. Directed Assembly of Bimetallic Nanoarchitectures by Interfacial Photocatalysis with Plasmonic Hot Electrons. In *Nanophotonic Materials XV*; International Society for Optics and Photonics: Bellingham, WA, USA, 2018; p. 19, doi: 10.1117/12.2321032.
41. Xinyin, S.; Frankel, D.J.; Hermanson, J.C.; Lapeyre, G.J.; Smith, R.J. Photoemission Studies of Ordered Pd Overlayers on Au(111): Implications for CO Chemisorption. *Phys. Rev. B* **1985**, *32*, 2120–2125.
42. Bligaard, T.; Nørskov, J.K. Ligand Effects in Heterogeneous Catalysis and Electrochemistry. *Electrochim. Acta* **2007**, *52*, 5512–5516.
43. Su, R.; Tiruvalam, R.; Logsdail, A.J.; He, Q.; Downing, C.A.; Jensen, M.T.; Dimitratos, N.; Kesavan, L.; Wells, P.P.; Bechstein, R.; et al. Designer Titania-Supported Au-Pd Nanoparticles for Efficient Photocatalytic Hydrogen Production. *ACS Nano* **2014**, *8*, 3490–3497.
44. Foerster, B.; Joplin, A.; Kaefer, K.; Celiksoy, S.; Link, S.; Sönnichsen, C. Chemical Interface Damping Depends on Electrons Reaching the Surface. *ACS Nano* **2017**, *11*, 2886–2893.
45. Forcherio, G.T.; Dunklin, J.R.; Backes, C.; Vaynzof, Y.; Benamara, M.; Roper, D.K. Gold Nanoparticles Physicochemically Bonded onto Tungsten Disulfide Nanosheet Edges Exhibit Augmented Plasmon Damping. *AIP Adv.* **2017**, *7*, 075103.
46. Boltersdorf, J.; King, N.; Maggard, P.A. Flux-Mediated Crystal Growth of Metal Oxides: Synthetic Tunability of Particle Morphologies, Sizes, and Surface Features for Photocatalysis Research. *CrystEngComm* **2015**, *17*, 2225–2241.
47. Gao, F.; Goodman, D.W. Pd-Au Bimetallic Catalysts: Understanding Alloy Effects from Planar Models and (Supported) Nanoparticles. *Chem. Soc. Rev.* **2012**, *41*, 8009–8020.
48. Lee, Y.W.; Kim, M.; Kim, Y.; Kang, S.W.; Lee, J.H.; Han, S.W. Synthesis and Electrocatalytic Activity of Au-Pd Alloy Nanodendrites for Ethanol Oxidation. *J. Phys. Chem. C* **2010**, *114*, 7689–7693.
49. Wang, B.; Tao, L.; Cheng, Y.; Yang, F.; Jin, Y.; Zhou, C.; Yu, H.; Yang, Y. Electrocatalytic Oxidation of Small Molecule Alcohols over Pt, Pd, and Au Catalysts: The Effect of Alcohol's Hydrogen Bond Donation Ability and Molecular Structure Properties. *Catalysts* **2019**, *9*, 387.
50. Song, H.M.; Anjum, D.H.; Sougrat, R.; Hedhili, M.N.; Khashab, N.M. Hollow Au@Pd and Au@Pt Core-Shell Nanoparticles as Electrocatalysts for Ethanol Oxidation Reactions. *J. Mater. Chem.* **2012**, *22*, 25003–25010.
51. Ksar, F.; Ramos, L.; Keita, B.; Nadjo, L.; Beaunier, P.; Remita, H. Bimetallic Palladium-Gold Nanostructures: Application in Ethanol Oxidation. *Chem. Mater.* **2009**, *21*, 3677–3683.
52. Zhu, L.D.; Zhao, T.S.; Xu, J.B.; Liang, Z.X. Preparation and Characterization of Carbon-Supported Sub-Monolayer Palladium Decorated Gold Nanoparticles for the Electro-Oxidation of Ethanol in Alkaline Media. *J. Power Sources* **2009**, *187*, 80–84.
53. Li, Y.; Hu, J.; Ma, D.; Zheng, Y.; Chen, M.; Wan, H. Disclosure of the Surface Composition of TiO_2-Supported Gold-Palladium Bimetallic Catalysts by High-Sensitivity Low-Energy Ion Scattering Spectroscopy. *ACS Catal.* **2018**, *8*, 1790–1795.
54. Engelbrekt, C.; Crampton, K.T.; Fishman, D.A.; Law, M.; Apkarian, V.A. Efficient Plasmon-Mediated Energy Funneling to the Surface of Au@Pt Core–Shell Nanocrystals. *ACS Nano* **2020**, *14*, 5061–5074.
55. Syrek, K.; Skolarczyk, M.; Zych, M.; Sołtys-Mróz, M.; Sulka, G.D. A Photoelectrochemical Sensor Based on Anodic TiO_2 for Glucose Determination. *Sensors* **2019**, *19*, 4981.
56. Dumortier, M.; Bosserez, T.; Rongé, J.; Martens, J.A.; Haussener, S. Combined Experimental-Numerical Analysis of Transient Phenomena in a Photoelectrochemical Water Splitting Cell. *J. Phys. Chem. C* **2016**, *120*, 3705–3714.
57. Gurudayal, G.; Chiam, S.Y.; Kumar, M.H.; Bassi, P.S.; Seng, H.L.; Barber, J.; Wong, L.H. Improving the Efficiency of Hematite Nanorods for Photoelectrochemical Water Splitting by Doping with Manganese. *ACS Appl. Mater. Interfaces* **2014**, *6*, 5852–5859.
58. Molina, L.M.; Benito, A.; Alonso, J.A. Ab Initio Studies of Ethanol Dehydrogenation at Binary AuPd Nanocatalysts. *Mol. Catal.* **2018**, *449*, 8–13.
59. Al-Zubeidi, A.; Hoener, B.S.; Collins, S.S.E.; Wang, W.; Kirchner, S.R.; Hosseini Jebeli, S.A.; Joplin, A.; Chang, W.S.; Link, S.; Landes, C.F. Hot Holes Assist Plasmonic Nanoelectrode Dissolution. *Nano Lett.* **2019**, *19*, 1301-1306.